THE TESTING AND VERIFICATION OF A NANOMEMBRANE BASED PRESSURE SENSOR FOR SMALL-SCALE UNDERWATER PRESSURE MEASUREMENTS

OMAR TALAKSI

Thesis submitted to the faculty of the Virginia Polytechnic Institute and State University in partial fulfillment of the requirements for the degree of

Master of Science
In
Aerospace Engineering

Wing F. Ng, Chair
Aurelien Borgoltz
Olivier Coutier-Delgosha

April 25, 2023
Blacksburg, VA

Keywords: MEMS, Underwater, Pressure Sensor

THE TESTING AND VERIFICATION OF A NANOMEMBRANE BASED PRESSURE SENSOR FOR SMALL-SCALE UNDERWATER PRESSURE MEASUREMENTS

OMAR TALAKSI

ABSTRACT

A MEMS piezoresistive pressure sensor provides a low-cost and accurate means of detecting and quantifying small-scale disturbances in underwater environments. A highly sensitive MEMS pressure sensor has been developed that can be packaged in two different ways – one in a cylindrical housing, and the other in a flexible, yet robust, strip configuration – enabling more freedom for the user to choose an option that fits their needs. The sensing element of each consists of four piezoresistive elements in a Wheatstone Bridge configuration arranged on a deformable buried-oxide layer, which is then bonded to a Silicon base layer with a hollow cavity carved using reactive-ion etching. Previous work has shown the survivability of these sensors in an underwater environment and also measurements of low frequency pressure changes due to flow and varying turbulence intensities. The present work is focused on evaluating these pressure sensors and testing the limits of the sensing element in the low, medium, and high frequency regime (<100Hz to >1kHz) to gain further insight into the performance.

Five experimental tests were developed and conducted to guide this research objective. The sensor responses under different flow conditions were measured and analyzed with selected filtering and resampling techniques to eliminate background noises. First, the sensors were calibrated to ensure their linearity and to determine their pressure sensitivities. Then, using bench-top testing rigs and a water tunnel, the sensor performance was evaluated in submerged environments when subjected to multiple small-scale flow disturbances across the tested frequency regime.

It was found that the present sensors are capable of providing more accurate measurements across a tested frequency regime of 0 to 20,000Hz when compared to other off-the-shelf products. Testing in submerged environment showed that the sensors are capable of detecting small-scale pressure fluctuations as a result of eddies which are evident in a Von Karman vortex street and a turbulent flow. Despite the presence of EMI noise within a water tunnel, the sensors demonstrated a decay of pressure fluctuations that is consistent with previous research in the field. Overall, the present work increases understanding of the sensors' performances across a broad range of frequencies and provides insight into potential uses and future work.

THE TESTING AND VERIFICATION OF A NANOMEMBRANE BASED PRESSURE SENSOR FOR SMALL-SCALE UNDERWATER PRESSURE MEASUREMENTS

OMAR TALAKSI

GENERAL AUDIENCE ABSTRACT

Pressure sensors are an important, if not the most important, measurement device available today. Pressure sensors play an integral role in the everyday lives for everyone around the world; from applications in medicine, aerospace, autonomy and computation, these sensors provide real-time feedback and help gain a deeper understanding of a system. However, with the technological advances in the Modern Age, there has been a growing need for smaller, cheaper, and faster sensors. As a result, engineers continued to improve sensor performance in the past century with new technologies. A micro-electromechanical system (MEMS) pressure sensor offers a low-cost and energy efficient method to quantify pressure fluctuations within a system.

This work focuses on evaluating the performance of three MEMS pressure sensors for use in a submerged environment to detect small-scale pressure fluctuations across a broad range of frequencies. Five different tests were conducted to investigate this research objective. The first three were performed in a controlled underwater environment from which direct conclusions could be made. The last two were performed in an uncontrolled underwater environment from which comparisons to literature and known phenomena were used to draw conclusions. A key result showed that the sensor measurements aligned with prior research in the field. Multiple data reduction techniques were also used during post-processing to ensure accurate data was being collected.

The studies showed that the developed MEMS pressure sensors provided the same capabilities as other commercially available pressure measurement devices, all the while displaying a higher sensitivity and broader frequency range. Furthermore, the survivability and robustness of the sensor was proven when subjected to large- and small-scale flow disturbances in a water tunnel.

ACKNOWLEDGEMENTS

First, I want to acknowledge my family, Farid, Ruksana, Ali, and Nadia Talaksi, for having my back every step of the way. Without their unconditional encouragement, love, and support, this would not have been possible. Thank you.

Next, I want to thank my advisor, Dr. Wing Ng, for his guidance and insights, for always pushing me, and for the opportunity to work on this project. I also want to acknowledge the team at NanoSonic Inc., Dr. Hang Ruan, Dr. Echo Kang, Mr. Albrey de Clerck and Mr. Noah Jones, for their willingness to help and whose teachings have molded me into a better engineer.

Finally, I want to express my sincere gratitude to Dr. Shuo Mao for his many contributions to this paper behind the scenes.

Table of Contents

List of Figures

List of Tables

THE TESTING AND VERIFICATION OF A NANOMEMBRANE BASED PRESSURE SENSOR FOR SMALL-SCALE UNDERWATER PRESSURE MEASUREMENTS

O. Talaksi[1], A. de Clerck[2], Y. Kang[2], N. Jones[2], S. Mao[2,3], H. Ruan[2,3], W. Ng[3]

[1]Department of Aerospace Engineering, Virginia Tech, Blacksburg, VA 24061
[2]NanoSonic Inc., 158 Wheatland Drive, Pembroke, VA 24136
[3]Department of Mechanical Engineering, Virginia Tech, Blacksburg, VA 24061

NOMENCLATURE

f	Frequency
Re	Reynolds Number
U, U_∞	Freestream velocity
d, D	Diameter
ν	Kinematic viscosity
St	Strouhal Number
TI	Turbulence intensity
u'	Fluctuating velocity signal
TI_p	Pressure turbulence intensity
p'	Fluctuating pressure signal
p_d	Dynamic pressure
E	Energy
X_T	Fourier transform
T	Time (s)

1. INTRODUCTION

As the world continues to venture into new eras of technological advancements, the improvement of sensors is paramount to stay current with modern progressions. Pressure sensors are widely used in many engineering applications [1,2,3] and as such there is a growing demand for smaller, cheaper, and more sensitive alternatives.

Since the discovery of piezoresistive effects evident in the elements of Silicon and Germanium by C.S. Smith in 1954, the practical applications of piezoresistive sensors have made significant progress [4]. Piezoresistive pressure sensors offer a smaller and lighter packaging when compared to their mechanical counterparts, and quickly became a favorable alternative due to their simplicity and low-cost fabrication method [4,5]. These sensors were later miniaturized and combined with electronics as microelectromechanical systems (MEMS) and are widely used in numerous fields today such as biomedical [5] and industrial [4]. A typical piezoresistive pressure sensor is made from a semiconductor material on which four piezoresistors are rigidly bonded in a Wheatstone Bridge configuration to a flexible membrane [6]. When the membrane is placed under a condition of an applied pressure, the membrane bends slightly due to the induced stress causing the resistance within one, two, or all four of the piezoresistors to change (depending on the circuit design) [7].

In past decades, MEMS technology has taken a great leap in their potential uses and applications. In recent years, new microfabrication technologies have allowed these devices to be miniaturized even further, which would not have been achievable using traditional engineering methods [5]. In turn, MEMS sensors have become even more applicable and some of the latest developments have shown MEMS technology can be used to mimic biological sensing systems, such as hair cells [5], leaf veins [8], and seal whiskers [9]. Fluid flow rate and direction sensors, which can accurately determine flow properties and patterns [5], are being replaced by a lower cost MEMS alternative which can achieve a much higher resolution [10].

For underwater vehicles, pressure sensors provide valuable information about water depth and flow conditions. In the simplest of forms, ships and submarines use a device called a pitometer to measure static and dynamic pressure differences to determine velocity relative to the oncoming water [11]. While this is a great method to obtain large-scale pressure difference measurements, when the ship's velocity is low, the pitometer struggles to produce an accurate result due to the minimal dynamic and static pressure difference [11]. For small-scale pressure measurements a more advanced technology is required, one that is able to provide a deeper understanding of flow characteristics such as small-scale velocity and pressure fluctuations. One technique being used throughout literature are acoustic doppler devices [11-13]. These devices measure the doppler shift of acoustic waves scattered by irregularities embedded in water [12] and are available in different sizes dependent upon the type of application and desired measuring range. However, they present major setbacks in their size, high complexity and cost [12].

As more technological advancements are made, there is in turn a rising demand for autonomous underwater vehicles (AUVs), whose abilities allow for autonomous and discreet operation throughout various applications such as geoscience and military [14]. For an AUV to successfully maintain a proper trajectory and react to any flow perturbations, it must be able to measure and compute the source and magnitude of any flow fluctuations [15]. As a result, onboard most AUVs is an inertial navigation system (INS), which consists of either a doppler velocimetry log (DVL) or an acoustic doppler current profiler (ADCP). The INS is responsible for estimating the position, velocity, and acceleration of the

AUV using a navigational technique known as dead reckoning [14]. However, both a DVL and an ADCP utilize the effects of acoustic scattering, in turn deeming them susceptible to failure in the event of any major flow disturbance [14]. ADCPs are used commonly to provide aiding to deep sea robots, but the results scale poorly when multiple vehicles are used since the update rate must be divided by the number of vehicles [16]. Both systems also rely heavily on external navigation sensors to provide accurate navigational estimates [16].

With these systems, an AUV is susceptible to the small- and large-scale flow fluctuations hidden within the complex underwater environments in rivers or oceans [15]. To mitigate any risk of these fluctuations presenting a navigational challenge to the vehicle, a rapid, durable, and nonintrusive method is required which can instantaneously quantify any flow disturbances [17]. One such method is a surface mounted MEMS pressure sensor. There are few studies present in today's literature that use a non-intrusive piezoresistive type pressure sensor to measure small-scale flow properties in a submerged environment, and even fewer that exhibit the durability and sensitivity to reliably measure small-scale disturbances in harsh environments.

A recent study involving surface mounted pressure sensors has proved a step in the right direction. In an attempt to mimic the lateral lines found on fish, Chambers *et. al* have shown that using an array of 16 miniature piezoresistive pressure sensors could potentially control the position of an underwater vehicle relative to structures in the flow [15]. Each MS5401-AM piezoresistive silicon micromachined sensor has a 240 mV = 1 bar (0.597 mV/inH_2O) sensitivity and an accuracy of +/- 2 Pa. The sensing element of the MS5401-AM consists of a silicon membrane with borosilicate glass wafer bonded under vacuum to the back side for reference pressure, and implanted resistors in a Wheatstone Bridge configuration make use of the piezoresistive effect under an applied pressure [18]. However, this sensor is sensitive to sunlight due to the strong photo effect of Silicon which heavily limits its applications [18].

An array of polymer MEMS pressure sensor arrays developed by Kottapalli *et al.* [19] can transduce underwater pressure variations generated by moving objects. Similar to the research done by Chambers *et al.* [15], this array of MEMS sensors uses a pressure gradient to mimic the lateral-lines on blind cave fish, whose disturbances can be used to detect movement. Each individual pressure sensor has a sensitivity of 90.5 mV/ms^{-1} (45.3 mV/inH_2O) and a resolution of 25 mm/s and operate in a piezoresistive manner [19]. Flow pressure variations cause the liquid crystal polymer (LCP) membrane to deflect resulting in an output voltage from the imbalanced external Wheatstone bridge circuit [19]. The feasibility of this sensor was proven through multiple proof-of-concept experiments, but this technology is yet to be commercially available.

In order to provide the user with a reliable, durable, accurate and precise method of quantifying underwater small-scale pressure measurements, the authors developed nanomembrane based pressure sensors to fill the previously mentioned voids left by other commercial products available today. As with any new technology, testing and verification of the device is paramount in order to be certain of its abilities. The performance of three sensors, centering around their accuracy and durability when subjected to a variety of different flow conditions and environments, will be evaluated throughout the following sections. One is housed in a cylindrical packaging and the other two in a flexible strip membrane configuration. The details of each sensor and the sensing element will be discussed further in the next section.

In this paper, five tests – sensor calibration, low frequency stir test, mid to high frequency speaker test, low frequency vortex shedding test and an encompassing turbulence decay test – were designed and conducted to expose these sensors to conditions of an applied pressure in different submerged environments and flow disturbances. The results were analyzed to (1) evaluate the response of each sensor in the low (<100Hz), medium (>100Hz, <1kHz) and high (>1kHz) frequency regime and (2) assess the sensor performance when subjected to flow disturbances in a turbulence environment.

2. SENSOR DESCRIPTION

The feasibility of these piezoresistive pressure sensors are evaluated throughout the following sections. All developed by NanoSonic Inc., one sensor is housed in a cylindrical packaging (referred to as 'NanoSonic Cylindrical Sensor' (NCS)), while the other two use a novel flexible strip packaging (referred to as 'NanoSonic Flexible Strip Sensor' (NFSS)). Two different packaging methods provide the user to choose an option that fits their needs – whether it be a through-hole pressure measurement, surface mounted pressure sensing array, or a combination of both.

Sensing Element

The fabrication process for each sensing element studied in this paper was identical, however, these prototypes are slightly different in properties. As seen in Figure 1, it consists of a silicon based layer which is bonded to a buried oxide (BOX) layer to which the four piezoresistive elements are arranged. A small cavity has been carved out of the Silicon base layer using deep reactive-ion etching (DRIE) to allow ample space for the deflection of the flexible membrane and a resulting imbalanced Wheatstone bridge configuration. Bonding the substrate to the Silicon base layer creates a hollow, sealed cavity. The sensing element has a 4 mm by 4 mm square base that is 405μm in height and a weight of 1 gram.

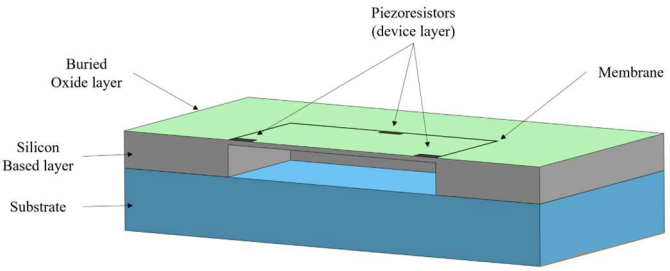

Figure 1: Cross-section view of the sensor sensing element

Cylindrical Sensor (NCS)

The NCS consists of four main components: the electrical connection, cylindrical housing, sensing element and protective HybridSil® coating, as shown in Figure 2.

The sensing element is housed underneath NanoSonic's HybridSil® coating whose environmental protection abilities have proven to decrease the likelihood of corrosion, leakage, and biofouling [20]. Together they are mounted flush with the tip of the probe. In this configuration, the sensor is powered by a GX12-6-6 pin Aviation plug and can be mounted using a through-hole installation. This installation method allows the sensing element to be flush with the exterior of a vehicle while hiding the sensor housing within, making it less susceptible to failure from environmental factors.

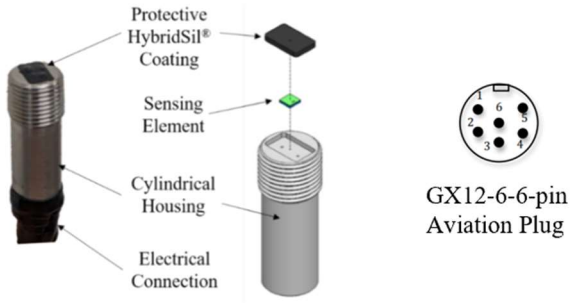

Figure 2: Photo (left) and CAD model (middle) of the cylindrical pressure sensor showing the four main components and GX12-6-6-pin Aviation Plug (right) [20]

Strip Sensor (NFSS)

The NFSS is designed in the flexible strip packaging configuration, in which the sensing element is bonded facing normal and outwards at the end of the flexible strip housing as seen in Figure 3. The fabrication process of the NFSS is proprietary to NanoSonic Inc.

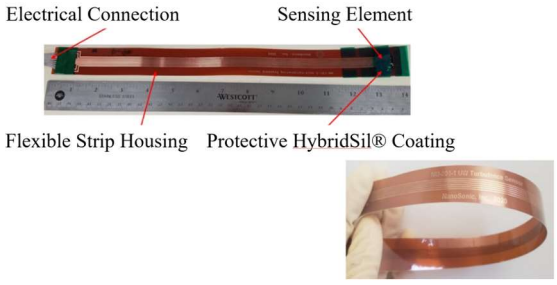

Figure 3: Detailed view of flexible strip packaging

In this configuration, the sensor can be mounted on and conform to non-flat or contoured surfaces, such as the exterior of underwater vehicles, allowing for a non-flow-intrusive pressure measurement device. Each sensor is powered by either a +3.3V battery or 120VAC (100 µW operation, 1 µW stand-by) power supply.

Sensor Specifications

The key specifications for each sensor are as follows:

1. Pressure measurement range: 0 – 6 in. H_2O
2. Frequency bandwidth: DC to >5MHz
3. Rise time: 0.112µs

These specifications allow the user to obtain small-scale underwater pressure measurements. The scope of this paper is limited to the sensor performance and sensitivity in the DC to 20kHz range.

3. SENSOR CALIBRATION

A relatively common mean of underwater pressure sensor calibration utilizes a water column to incrementally increase water pressure atop of a sensing element [21]. The static calibration test was conducted not only for calibration purposes, but also to determine the pressure sensitivity for both the cylindrical and flexible strip packaged sensors. The linearity and sensitivity of each sensor is also investigated and discussed.

3.1 Test Set Up

As presented in Fig. 4, the water column was designed as an empty rectangular chamber with a base measuring 1" x 1" and a height of 10". The cylindrical sensor was mounted to the base of the water column such that the sensing element was facing vertical, as shown in Figure 4a. Both flexible substrate sensors were mounted in a similar fashion, with the sensing element at the base and facing vertical, as shown in Figure 4b. The data was recorded using a Picoscope oscilloscope at a sampling rate of 8.9MHz. Static pressure calibration was performed to observe the DC performance of each sensor. Data was recorded as the water height was increased from 0" to 5" in 0.25" increments, then 0.125" increments up to 6". The water was slowly dispensed into the column using a pipette at a height close to 0". Data recording began once any surface fluctuations had decayed and the water was effectively stagnant.

3.2 Results and Discussion

The static calibration result is shown in Figure 5. All three tests suggest an R^2 value higher than 0.985, demonstrating excellent linearity of the Nanosonic sensors. In addition, each sensor displays a sensitivity higher than 289.5 mV/inH_2O, vastly surpassing the sensitivity of both previously mentioned sensors obtained from literature [15,18,19]. As previously stated, the sensing elements of

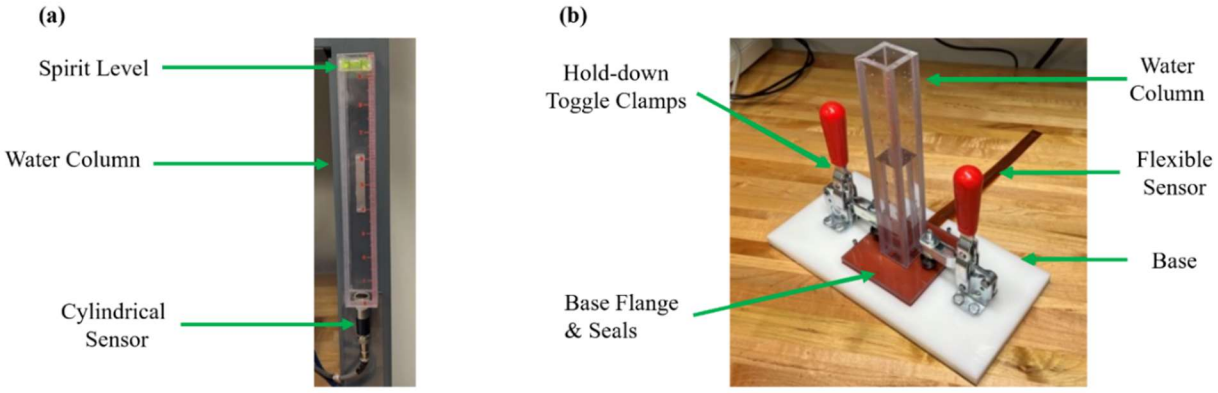

Figure 4: Detailed view of (a) Cylindrical sensor water column testing rig, (b) Flexible substrate sensor water column testing rig

the NCS, NFSS 1 and NFSS 2 are each slightly different, thus resulting in a different calibration curve for each sensor.

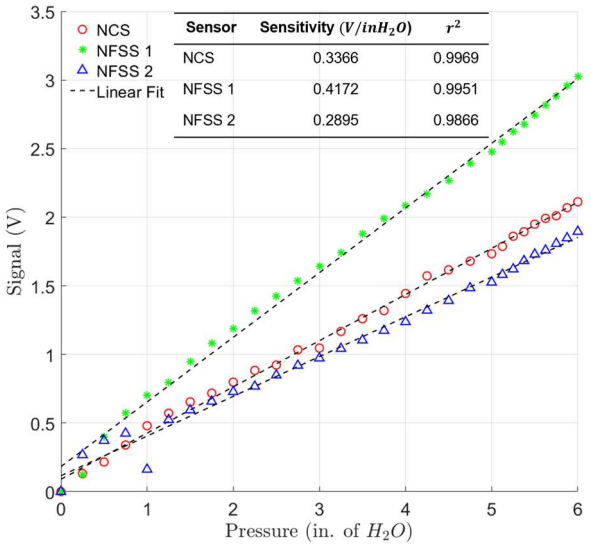

Sensor	Sensitivity (V/inH_2O)	r^2
NCS	0.3366	0.9969
NFSS 1	0.4172	0.9951
NFSS 2	0.2895	0.9866

Figure 5: Static calibration results for the NCS, NFSS 1 and NFSS 2. The table above shows the sensitivity of each sensor and the corresponding correlation coefficient

4. STIR TEST

In the stir tests, three different stirring devices were employed to generate low frequency flow disturbances (< 100Hz) near the sensors to test their response in a low frequency and submerged environment.

4.1 Test Set Up

Three different stirring devices were designed and 3-D printed using ABS for this study: a 2-arm stirrer, a 3-arm stirrer, and a 3-blade propeller, as shown in Figure 6.

Figure 6: Three-arm stirrer (left), two-arm stirrer (middle) and 3-blade propeller (right)

Figure 7 shows the experimental setup. The test was carried out in a deionized water tank. In each test, one of these stirring devices was installed 2" below the water surface facing downwards and ran at 4Hz, creating a low frequency disturbance underwater.

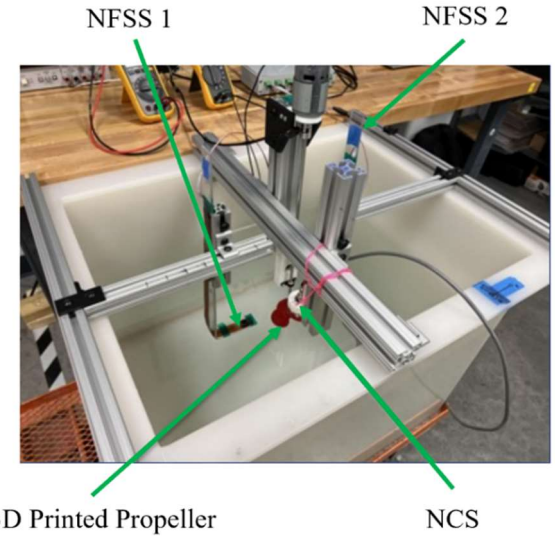

Figure 7: Stir test set-up including 3D printed propeller and 3 pressure sensors

The sensor was submerged underneath the water at the same depth as the stirrer, facing downwards, 1" away from the perimeter of the stirrer. Moreover, to study the effect of sensor locations, the sensor was fixed at variable distances from the propellers in 1-inch increments. A PicoScope was used to record the sensor output at 8.9MHz.

4.2 Results and Discussion

Figure 8 displays the response of NFSS 1 in the frequency domain in the form of a power spectral density plot in response to the three different stirring devices. For better visualization, a 100kHz low-pass filter and a sample point moving average filter were applied to each data set. The maximum frequency under study is 100Hz and therefore the raw data was further downsampled to 200Hz (from an original sampling rate of 8.9MHz) during data reduction.

A 200Hz sampling rate determines a Nyquist range of 100Hz, allowing for all relevant data to be captured [22]. A clear shift of peak can be seen between the responses to a 2- and 3-arm stirring device. At approximately the same rotational speed (4Hz), the 3-arm stirrer and 3-blade propeller induce similar frequency responses, peaking around 11.7 and 10.6Hz respectively. Both are approximately the rotational speed multiplied by a factor of 3 as expected, as each sensor is detecting the passing of each arm/blade. The 2-arm frequency differs more significantly, inducing a frequency response of 8.6Hz, following the previously explained reasoning.

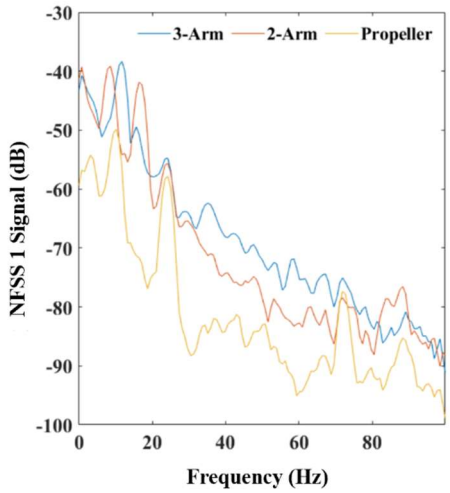

Figure 8: NFSS 1 power spectral density plot in response to the three different stirring devices. More energy is contained within a higher frequency when measuring the rotation of a stirrer/propeller with more arms/blades.

The response of NFSS 1 was tested at different distances from a 2-arm stirrer, with the results shown in Figure 9. Each test displays approximately the same peak frequency near 8.6Hz but decreasing power with increasing distance. 0" away from the stirrer, the measured peak-to-peak response is 0.044 inH_2O, and at 4" away the measured peak-to-peak response is 0.003 inH_2O. Despite the decayed excitation, the sensor can generate the correct frequency response.

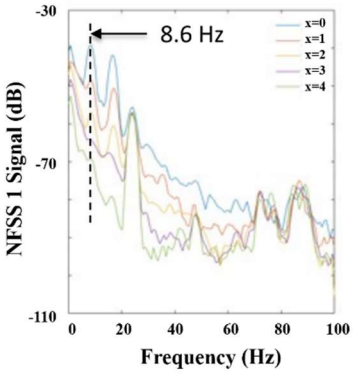

Distance from Stirrer (*in.*)	Peak-to-Peak (*in. H_2O*)
0	0.044
1	0.017
2	0.004
3	0.003
4	0.003

Figure 9: Sensor 4 response at each location; power spectrum (left), peak-to-peak vs. x-location (right)

Next, the two flexible strip sensors, NFSS 1 and NFSS 2, were placed equidistant from, but on opposite sides of the stirring device. Then the 2-arm and 3-arm stirrers were driven by a 4Hz motor to investigate the responses of the two sensors. Figure 10 shows the differing sensor response when using a 2-arm or 3-arm stirrer. For the 2-arm stirrer, the sensor signal responses were in-phase, and for the 3-arm stirrer, the sensor signal responses were out-of-phase.

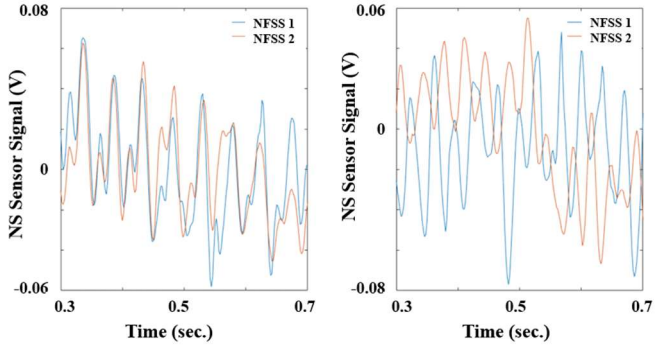

Figure 10: NFSS 1 and NFSS 2 response for a 2-arm stirrer (left) and a 3-arm stirrer (right)

This is a key expectation which indicates each sensor was individually detecting the passing of each blade. The fluctuation of each sensor response was then converted to a pressure reading to further characterize the sensor performance. Table 1 shows the estimated pressure fluctuation detected by each sensor.

Table 1: Estimated pressure fluctuations (in. H_2O) in response to both stirrers

Sensor	2-Arm	3-Arm
NFSS 1	~0.04	~0.03
NFSS 2	~0.02	~0.01

Each sensor detected an estimated pressure fluctuation of at least 0.01 in. H_2O, and at most 0.04 in. H_2O, which surpasses the sensitivity values of similar sensors, both listed in Section 1 [15,18,19].
The different tests contained within this section were successful in characterizing each sensor's performance in the lower frequency range. The frequency response of each sensor is close to what was expected for different numbers of blades on the stirrer/propeller, while also displaying the sensitive properties of the sensing element itself. Again, the sensitivity of the NCS, NFSS 1 and NFSS 2 are also found to be higher than their competitors.

5. MID TO HIGH FREQUENCY SPEAKER TEST

A series of speaker tests were conducted to determine the mid to high frequency response of the pressure sensors

under study. Tested against reference signals in the ranges of 600-20kHz, the response of each sensor was measured against a commercial off the shelf hydrophone, H2A-XLR Hydrophone developed by Aquarian Audio Products. An underwater speaker, Lubell Labs LL916C Pistonic Piezoelectric Underwater Speaker, was used to transmit said reference signals and a PicoScope oscilloscope was used for the reference signal generation as well as data acquisition.

5.1 Supplementary Equipment

H2A-XLR Hydrophone – Developed by Aquarian Audio Products, the H2A-XLR hydrophone acted as a control throughout this experiment, offering vital information for the verification of the response of the NanoSonic sensors. This hydrophone offers omnidirectional response and a useful range of 10-100kHz with a sensitivity of 1 V/µPa [23]. In order for proper operation, a Zoom H4n Pro 4-Track Portable Recorder was used to supply the hydrophone with a 48V phantom power.

Lubell Labs LL916C Pistonic Piezoelectric Underwater Speaker – The Lubell Labs LL916C underwater speaker was used to transmit specific reference signals to the NanoSonic sensor and hydrophone. The LL916C is cage-mounted and relatively light weight, which allowed for the easy placement at the bottom of the water tank. With a frequency response range of 200-23kHz, this speaker proved perfect for the needs of the current experiment, offering the capability to transmit the necessary mid to high frequency reference signals [24]. A Lubell Labs AC series transformer box was also needed to ensure the speaker provides broadband performance as well as current limiting and electrical isolation for increased safety measures [24].

A Picoscope oscilloscope was used to generate any reference signals and also for data acquisition. Picoscope oscilloscope software allows for real-time monitoring of the response of the speaker, hydrophone, and pressure sensors; this data was collected and processed in MATLAB.

5.2 Test Set Up

As shown in Figure 11, this experiment was set up in a 24” x 20” x 18” plastic tub. The tub was filled with 12” of de-ionized water, and the speaker was centered at the bottom facing upwards. One NCS and two NFSS were used throughout this test. The sensors and hydrophone were lowered into the water using multiple 80/20 beams. While the LL916C speaker and three pressure sensors were connected directly to the Picoscope oscilloscope, the hydrophone was first wired to the Zoom H4n power supply and then to the oscilloscope. The speaker, hydrophone, and pressure signals were recorded at a sampling rate of 40kHz using the Picoscope oscilloscope data acquisition software. The seven reference signals used were: 600, 750, 5700, 10000, 12000, 15000, and 20000Hz. Each reference signal was sent directly to the speaker while the responses of the hydrophone, and each pressure sensor were recorded.

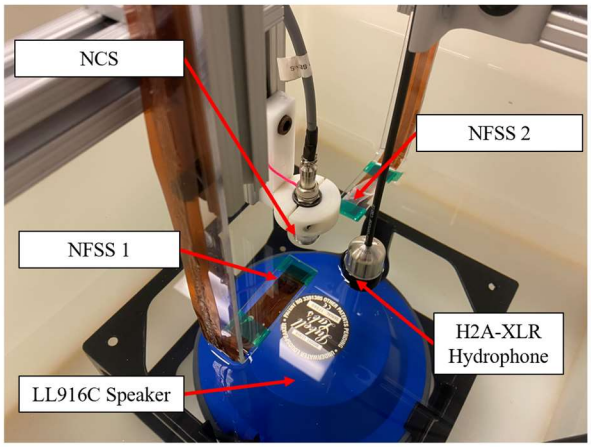

Figure 11: Picture of the Test Setup including the three NanoSonic pressure sensors, H2A-XLR hydrophone and LL916C speaker

5.3 Results and Discussion

Within this experiment, multiple tests were conducted to ensure the accuracy and validity of the sensors in the mid to high frequency range of 600-20kHz. Both the AC and DC response of each sensor were evaluated through three different tests: a frequency domain test, a reference signal amplitude test, and a DC offset test.

5.3.1 Frequency Domain Test

The data obtained was processed in MATLAB, and Fast-Fourier Transform (FFT) plots were drawn to determine the frequency response of the sensors. The extracted data from the speaker, sensors, and hydrophone were manipulated using the built-in FFT function in order to display the response of each in the frequency domain. Each sensor exhibited a behavior very similar to the hydrophone and speaker input. For each tested reference signal, the hydrophone and pressure sensors presented a peak at the same frequencies on the FFT, exhibiting that they were picking up the correct corresponding input frequencies. To compile this data, the FFT for every reference signal was plotted to display the overall frequency response, as seen in Figure 12.

Each sensor response displays seven peaks across the x-axis, corresponding to the seven corresponding input frequencies. They suggest that the sensors are detecting the different input frequencies that were transmitted through the speaker. The sensor response when compared to the response of the hydrophone makes it clear that the two align at every peak; a strong indication that the

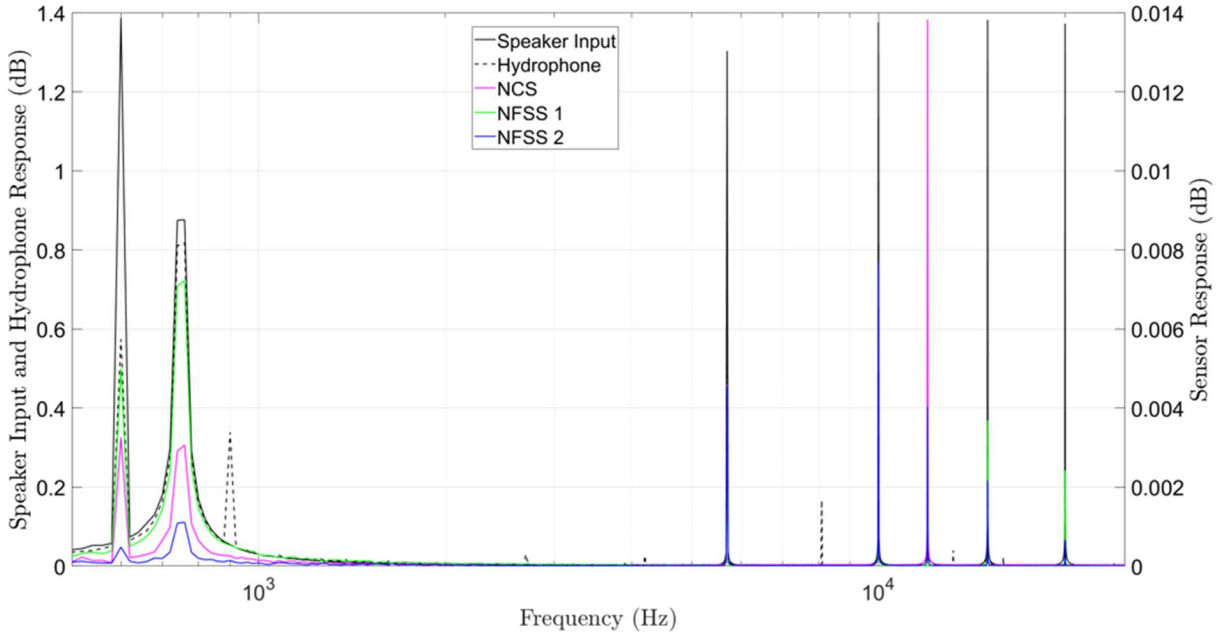

Figure 12: FFT data on a semi-log-x plot of the speaker input, hydrophone and three NanoSonic sensors response to the seven reference signals

sensors performance in the mid to high frequency regime can be verified.

Two more peaks can be seen in the response of the hydrophone at signals that were not tested, which is more indicative of the hydrophone performance than that of the sensors.

5.3.2 Changes in Amplitude

The sensors' frequency response was also tested against a change in the reference signals' amplitude. Three different excitation amplitudes of 30, 50, and 100 mV were used throughout this test. Table 2 displays the peak-to-peak response of the sensors as the speaker input amplitude is changed. As can be seen from Table 2, there is a clear linear increase in the peak-to-peak response of the NanoSonic sensors as the speaker input amplitude is increased, as expected. This relationship is indicative of the AC performance of the pressure sensors – the amplitude of the fluctuating signal component of the sensor response is directly correlated to the speaker input amplitude.

Table 2: The peak-to-peak response of each pressure sensor as the speaker input amplitude is changed

	Peak-to-Peak (mV)		
Speaker Input Amplitude	NCS	NFSS 1	NFSS 2
30	2.923	6.5	1.465
50	5.28	11.72	2.063
100	9.907	22.76	3.53

5.3.3 DC Offset Test

An additional test was performed to observe the DC offset of the pressure sensors. To measure flow parameters such as depth, it is crucial that an underwater pressure sensor has the capability to measure DC signals to capture static pressure measurements. Within this test, all pressure sensors were moved down 1-inch in order to test the DC response as they were submerged deeper in the water. The data obtained for this test can be seen in Figure 13. A clear upwards shift can be seen after the sensors are submerged 1-inch deeper in the water which corresponds to the increase in static pressure. The DC offset that is evident

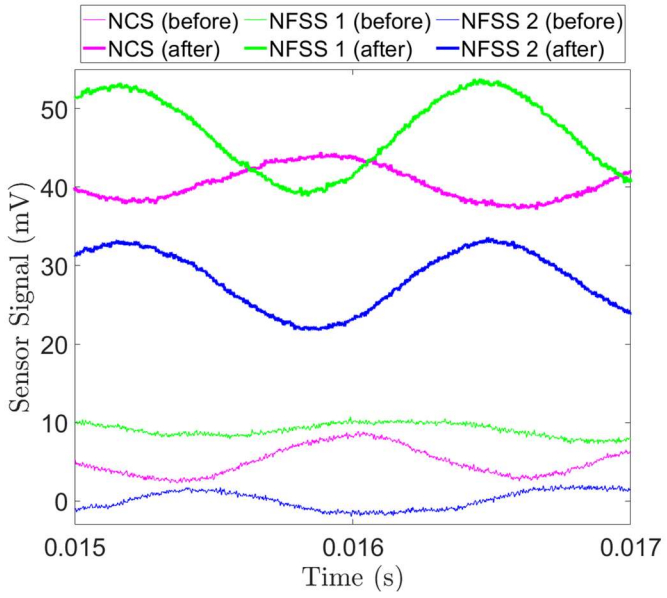

Figure 13: Recorded data at 750Hz and 50 mV input frequency and amplitude for the pressure sensor frequency response, before and after all sensors were shifted down 1"

is what separates the sensors from the hydrophone, as a hydrophone can only detect AC signals.

The completion of this test provides valuable insight into the performance of the sensors in the mid to high frequency range. The three pressure sensors showed great performance across a broad range of frequencies between 600-20kHz. It is clear from Figure 12 that each sensor detects the exact corresponding input frequencies across the tested frequency regime, and the sensor responses match the response of both the speaker and hydrophone. The peak-to-peak response of each sensor increases in a linear fashion as the input amplitude is increased, as expected. The sensors also display a DC offset as they were submerged 1-inch deeper in the water, indicating their ability to provide static pressure measurements.

6. VORTEX SHEDDING

Using a water tunnel at Virginia Tech, a test was conducted to determine the frequency response of NFSS 1 against an oncoming Von Karman vortex street. This was the first test performed in an environment of a known shedding frequency.

6.1 Theory

There has been much research in the recent decades regarding the flow around a circular cylinder when placed perpendicular to a steady stream [25]. The different flow patterns that can be observed around the body are controlled by the Reynolds number, $\mathrm{Re} = U_\infty D/\nu$, where ν is the kinematic viscosity of the fluid which is moving at flow speed U_∞ around a cylinder of diameter D [26]. When the Reynolds number exceeds some critical number (cited in [26] as Re ~ 40), the wake behind the cylinder becomes unstable and eddies successfully leave the cylinder in an alternating fashion with a very regular spacing [26, 27]. In this flow pattern, one vortex will grow larger than the other, eventually causing a separation of its shear layer and then the shedding of the vortex [27]. Consequently, upon the shedding of this vortex, the previously smaller vortex will continue to grow in size until it, too, separates from its shear layer and sheds [27]. This vortex shedding pattern is known as a Von Karman vortex street.

If a velocity (or pressure) measurement device is placed within a Von Karman vortex street, one would see a periodic oscillation with one cycle corresponding to the vortex of the same sign [26]. The frequency of this oscillation can be defined by the Strouhal relation:

$$f = \frac{StU_\infty}{D} \quad (1)$$

Where St is the Strouhal number, U_∞ is the freestream velocity, and f is the predominant frequency of the vortex shedding. The Strouhal number, which is found to be a nearly constant value of St ~ 0.22 across the span of the subcritical Reynolds number range of 300 – $2.5*10^5$, relates the frequency of the vortex shedding to the flow and circular cylinder parameters [28]. Being reported by many authors, it is found to be a weak function of Reynolds number throughout literature [27].

6.2 Test Set Up

The water tunnel which was used throughout this test features a test section of size 6” x 6” x 18”. With a 1.5 hp centrifugal pump to drive the water, the flow is capable of reaching a maximum speed of 0.52 m/s. Before the water enters the test section, it passes through a plastic honeycomb section and three 60% porosity screens designed to straighten the flow and make it more uniform. The test set up and water tunnel can be seen in Figure 14.

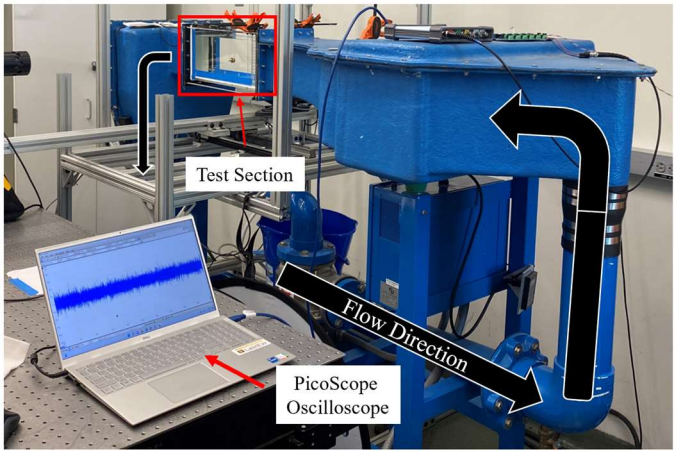

Figure 14: A picture of the test set up, showing the water tunnel, water tunnel test section and PicoScope oscilloscope

A 0.750” diameter circular cylinder was mounted at the mid-height of the test section perpendicular to the flow direction for predictable vortex generation. It should be noted that the water contained within the tunnel was heavily polluted with 250-300 µm diameter polyethylene seed particles to aid in the use of a particle shadow velocimetry (PSV) system.

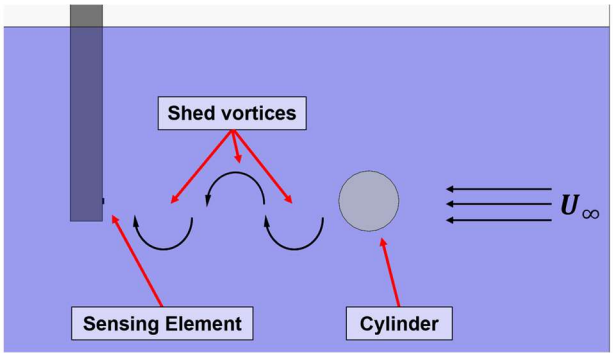

Figure 15: Drawn diagram of the water tunnel test section

Once the set up was configured, NFSS 1 was mounted on an 80/20 beam with the sensing element normal to the flow direction, and lowered into the flow to a depth of 3" (mid-height) as seen in Figure 15. The water tunnel flow speed was varied between 0.16, 0.33 and 0.52 m/s to measure the effects of a varying flow speed on the sensor response. Data were recorded using a PicoScope oscilloscope at a sampling rate of 8.9MHz.

6.3 Results and Discussion

As mentioned, flow over a blunt body at a sufficient Reynolds number leads to an unsteady flow separation and the subsequent shedding of a predictable and repeating pattern of swirling vortices.

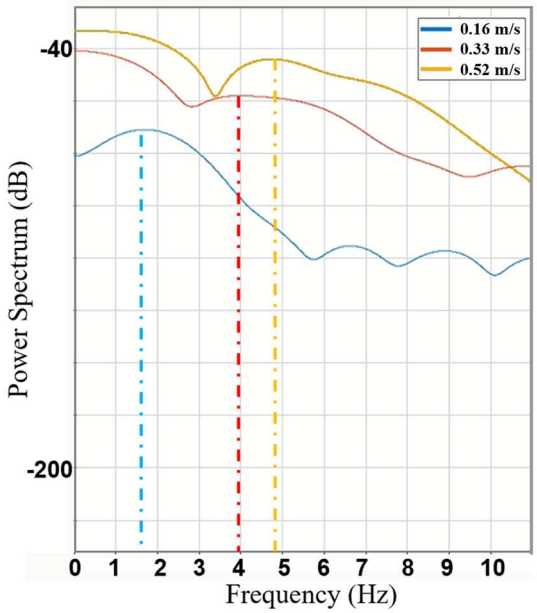

Figure 16: Power spectrum drawn by NFSS 1 in response to a vortex street at different flow speeds

Using the Strouhal relation, it is quite simple to determine the expected frequency of vortex shedding from the cylinder. The Reynolds number of the cylinder at the maximum flow speed of 0.52 m/s is Re = 11076, well below the subcritical Reynolds number range, allowing for the Strouhal number of 0.22 to be used in the relation [27].

Once data were obtained, evaluating the power spectrum drawn by the sensor in response to the vortex street generated at the different flow speeds will denote the dominant frequencies detected. Figure 16 shows the power spectrum as well as the peak frequencies. Each peak frequency corresponds to the frequency of vortex shedding observed by the sensor and can be compared to the expected vortex shedding frequency (calculated using Equation 1), as arranged in Table 3.

Table 3: Flow speed vs. expected and observed vortex shedding frequency

Flow Speed (m/s)	Expected Vortex Shedding Frequency (Hz)	Observed Vortex Shedding Frequency (Hz)
0.16	1.85	1.75
0.33	3.79	4.00
0.52	5.99	4.97

It is clear that the observed vortex shedding frequency continues to increase as the flow speed increases as expected. Additionally, the fairly linear increase in the observed value corresponds with the expected value with an average error of ~9%. This proves a step in the right direction in terms of the sensor's accuracy and sensitivity. Testing the sensor in an environment such as a water tunnel is of importance in order to verify its performance in a more "true to life" environment. The polluted water contained within the tunnel can heavily distort sensor readings and lead to potential sensor damage – even so, the sensor showed great resilience to this obstacle, providing insight into NanoSonic's HybridSil® coating and the overall durability of the sensor. The relationship between flow speed and observed vortex shedding frequency aligns with the correlations found in literature [25-28] and the Strouhal relation, further verifying the sensors abilities to detect low frequency pressure fluctuations. The vortices generated by a Von Karman vortex street are generally larger and typically observed at lower frequencies relative to, say, the vortices generated within freestream turbulence. As such, the results of another test will be discussed and investigated to measure higher frequency disturbances to ensure the sensor's capability in this aspect.

7. TURBULENCE DECAY

An experiment was conducted to simulate the mounting of a NanoSonic Flexible Strip Sensor (NFSS 2) on the surface of an underwater vehicle and evaluate its performance under more realistic conditions. The same water tunnel from the previous section was utilized to generate a flow velocity, and the sensor was carefully positioned at different locations within its test section to obtain measurements in the freestream and behind a turbulence generating grid. The acquired pressure fluctuations were carefully evaluated, in the presence of strong EMI noise from the water pump, to derive meaningful insights regarding the functionality of the sensor.

The objectives of this test were to:

1. Observe sensor response when mounted normal to the flow direction on a flat-faced probe
2. Use the sensor to quantify pressure fluctuations in a water tunnel test section, in both the freestream and behind a turbulence generating grid
3. Evaluate sensor durability

The outcomes of this test will establish the groundwork for future experiments that will further validate the sensor's ability to quantify small-scale pressure fluctuations.

7.1 Test Set Up

To generate turbulence (and therefore pressure fluctuations) in the water tunnel test section, two grids were designed following the aid of multiple research papers. The grid porosity, mesh width, and rod diameter of the first grid (referred to as 'Grid 1') were selected to be 0.58, 0.403", and 0.096", respectively based on the research of Roach, Yao, Kurian and Fransson [29-31].

The grid porosity, mesh width, and rod diameter of the second grid (referred to as 'Grid 2') were calculated in a similar fashion, and selected to be 0.66, 0.403", and 0.076", respectively. These grid designs were modelled in SolidWorks and 3D printed using ABS material.

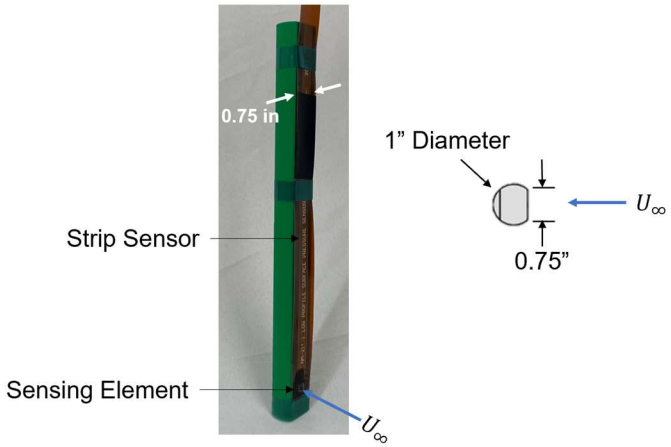

Figure 17: Strip sensor mounted on designed probe, noting the sensing element and direction of flow

As seen in Figure 17, the sensor probe was designed as a 1" diameter cylinder with a 0.75" flat face for mounting the flexible strip sensor. The design was modelled in SolidWorks and 3D printed using ABS material.

This experiment used the same water tunnel at Virginia Tech as discussed in Section 6. For this test however the cylinder was removed from the test section which allowing the sensor to move in the streamwise direction across the entire tunnel.

As seen in Figure 18, the flexible strip sensor is mounted on the 3D printed mounting device and lowered to a flow

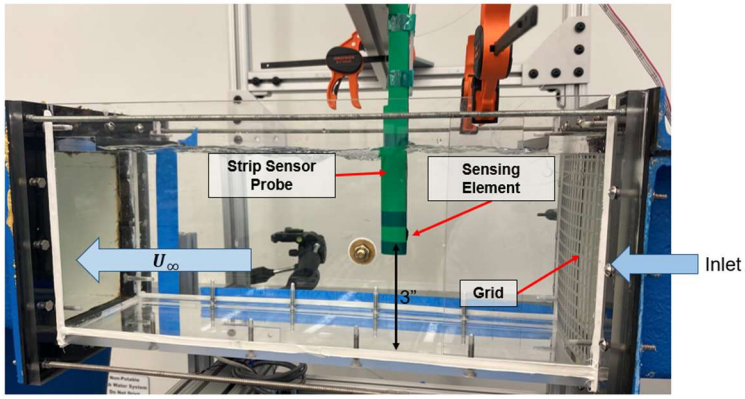

Figure 18: Side view of the water tunnel test-section, noting the sensing element and turbulence generating grid

depth of 3", with the sensing element normal to the oncoming water. The flow speed was kept constant at a value of 0.52 m/s. In order to account for the impact of the EMI noise from the water tunnel pump on the measurements, data was first obtained with the sensor placed 1" above the water (i.e., sensor not in water) when the pump was turned on. Then the grid was placed at the test section entrance and fixed using CNC cut plexiglass mounts which were clamped down against the test section walls. The sensor was moved axially between 1" – 12" downstream of the grid in 1" increments and the response at each downstream location was measured. At each location, the grid was removed from the flow and an additional measurement was obtained, which corresponds to the freestream condition with the grid out. Data were recorded using a PicoScope oscilloscope.

7.2 Results and Discussion

The data were processed, analyzed and plotted in MATLAB. First, the obtained voltage data was converted to a pressure reading using the sensor's calibration curve. Then, in an effort to reduce the levels of EMI noise from the water pump present in the acquired measurements and to expedite computation time, the pressure data was down sampled. Analysis of the power spectrum obtained with the sensor out of the water and the pump turned on revealed a discernible impact of EMI noise, emanating from the water tunnel pump, beyond 75Hz. As seen in Figure 19, the power spectrum plot displays irregular peaks beyond 75Hz, which are clear indicators of significant EMI noise interference in the measurements. Therefore, the Nyquist frequency for the measurements was established to be 75Hz, and it was determined that a sampling rate of 150Hz represented the upper limit of reliable measurement capability for the sensor throughout this test. For a further discussion on how this sampling rate was chosen and the effect of the water tunnel pump, see Appendix sections C and D.

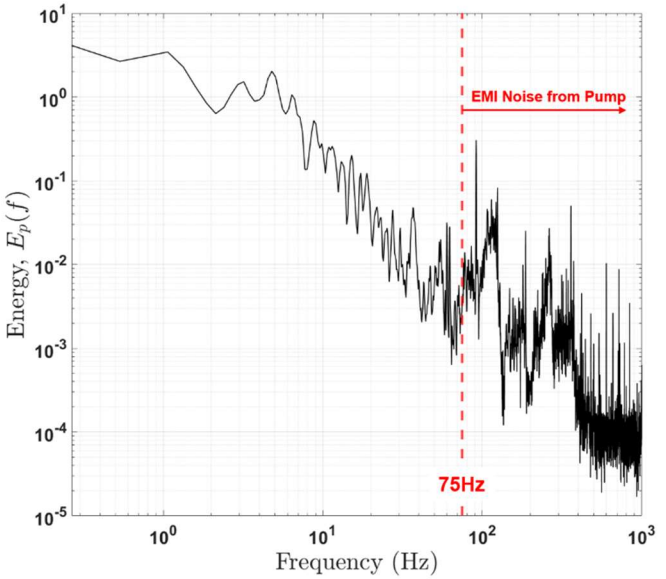

Figure 19: The calculated power spectrum 5" downstream of the turbulence generating grid

The reasoning behind this test was heavily drawn from the theory of turbulence decay, which states that as a flow moves away from a source of turbulence, the turbulence within it will gradually decrease. Consequently, it is reasonable to expect a reduction in pressure fluctuations as the sensor is moved further downstream. Turbulence intensity is one of the parameters commonly employed to gauge turbulence decay, and its equation is as follows:

$$TI = \frac{std(u')}{U_\infty} \quad (2)$$

Where $std(u')$ is the standard deviation of the fluctuating velocity signal, u', and U_∞ is the freestream velocity. However, because the sensor measures pressure, converting these values to a velocity through Bernoulli's equation will only introduce uncertainties that cannot be accounted for. Therefore, the equation for turbulence intensity was suitably modified to be expressed solely in terms of pressure as:

$$TI_p = \frac{std(p')}{p_d} \quad (3)$$

Where $std(p')$ is the standard deviation of the fluctuating pressure signal, p', and p_d is the dynamic pressure based on the flow velocity. Values calculated using this equation will be referred to as the pressure turbulence intensity.

Although downsampling the data to 150Hz significantly reduced the noise present in the signal, a considerable portion of the turbulence data was also eliminated. Therefore, to focus on the trend of the data rather than the absolute magnitude, each pressure turbulence intensity measurement was normalized based on the largest value obtained (measured at a downstream distance of 1"), resulting in a range between 0 and 1 for each value. Grid 1 was placed at the test section entrance, and the pressure turbulence intensity values obtained from four repeating trials. These results can be seen in Figure 20.

The calculated curve fit for the pressure turbulence intensity data without the grid is $TI_p = 0.15x^{-0.16}$, where x is the downstream distance from the entrance of the test section (and where the grid was mounted) in inches. The calculated curve fit for the pressure turbulence intensity data when the grid was in the flow is $TI_p = 0.78x^{-0.64}$, where x is the downstream distance from the entrance of the test section in inches. As seen in Figure 20, it is clear that the pressure turbulence intensity values are higher behind the turbulence generating grid than when in the freestream, indicating larger pressure fluctuations. In addition, the negative exponent evident in the calculated curve fits for both cases are indicative of a decreasing trend.

As previously stated, the theory of turbulence decay suggests that turbulent eddies within a flow will gradually

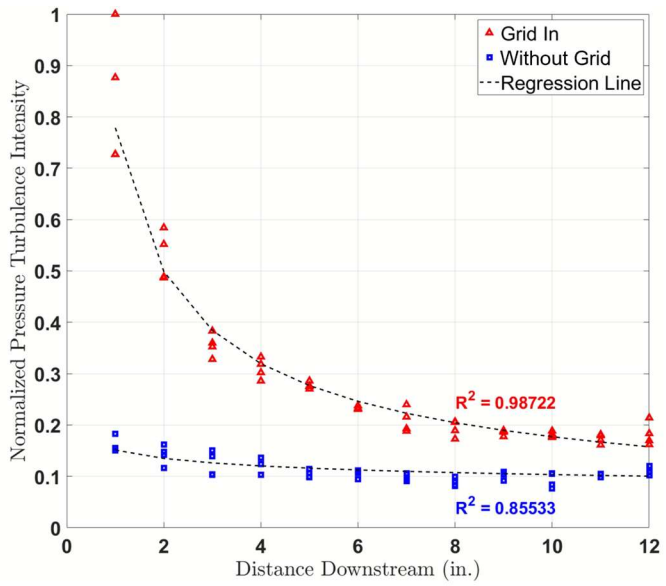

Figure 20: Streamwise pressure turbulence intensity data without grid (blue) and behind the turbulence generating grid (red)

dissipate as the flow moves further away from a source of turbulence. Thus, smaller pressure fluctuations are expected as the sensor is moved downstream. Therefore, the decreasing trends seen in Figure 20 align with the theory of turbulence decay as anticipated. Both regression lines also show a very high R^2 value, indicating a large correlation between the proposed fit and the obtained data. Ultimately, a key result showed that the sensor consistently detected larger pressure fluctuations behind the grid and a decay of these pressure fluctuations as it was moved downstream, throughout four repeating trials

which demonstrates repeatability in the obtained measurements.

With all variables held constant, Grid 1 was then interchanged with Grid 2. The only difference between both grids is the rod diameter, with the diameter of the rods in Grid 1 being 0.0205" larger than that of Grid 2. Although this is a seemingly miniscule difference, the turbulence patterns produced by each grid will be different, with the larger rods in Grid 1 shedding slightly larger turbulent eddies. This means that the pressure fluctuations generated by Grid 1 should be slightly larger when compared to the pressure fluctuations generated by Grid 2. This was a key expectation of this test, and the obtained results can be seen in Figure 21.

From these results, it is clear that the sensor detected higher pressure fluctuations behind Grid 1. When comparing the two data sets, the data obtained behind Grid 1 is higher relative to the data obtained behind Grid 2, as expected. Therefore, it can be seen that when changing only the grid geometry, the sensor measured smaller pressure fluctuations as the rod diameter was decreased.

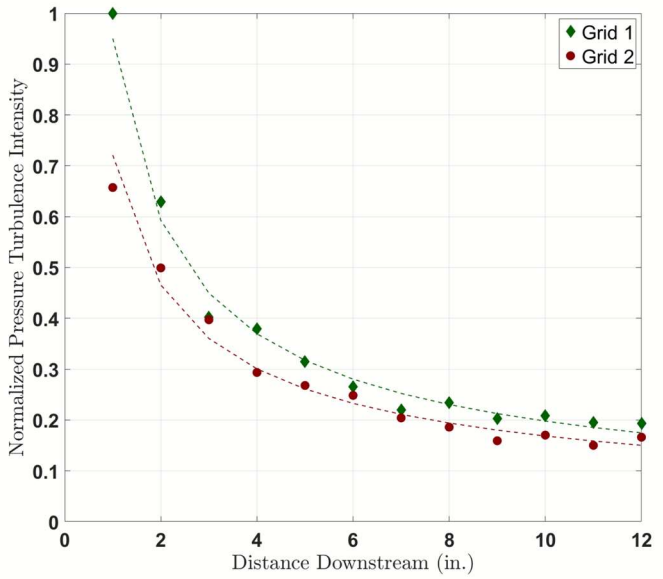

Figure 21: Grid 1 vs. Grid 2 results

This test was a crucial step to not only determine the performance of the sensor, but also determine its limitations. The same water tunnel was used as in Section 6, and therefore large amounts of seed particles were present in the flow. The NFSS 2 was constantly being exposed to this contaminated flow for prolonged periods which provides promising insights into its robust design and HybridSil® coating.

One of the primary objectives of this experiment was to evaluate the performance of the sensor when mounted on a probe that simulates its placement on the surface of an underwater vehicle. In this configuration, the results have shown the sensors capability to measure pressure turbulence intensity data based on small-scale pressure fluctuations. Evaluating the obtained pressure data when behind Grid 1 and without Grid 1, it is evident that the sensor measured higher pressure fluctuations behind the turbulence generating grid. This result was consistent throughout four different trials, demonstrating that the experiment is repeatable. In addition, it was found that when changing the grid geometry, the measured pressure fluctuations decreased as the rod diameter decreased.

However, there are quite a few sources of error that impacted the results of this test, the first of which being the shape of the sensor probe, which can be seen in more detail in Figure 22.

The 0.75" flat face for the sensor mount is very large relative to the 0.07" x 0.07" active sensing nanomembrane. The presence of this blunt and flat face can change the flow field around the sensing element and can create flow disturbances that cannot be accounted for. Unfortunately, this sensor probe shape was found to be the most efficient design for a sensor mounted on the surface of an underwater vehicle.

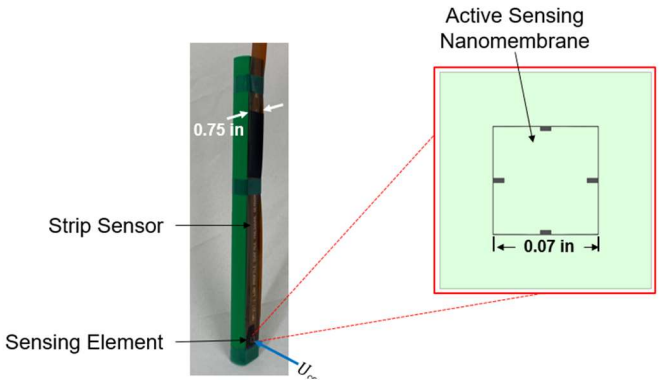

Figure 22: Isometric view of sensor probe (left) and active sensing nanomembrane (right)

The EMI generated by the water tunnel pump, lighting fixtures and electrical circuits throughout the lab can also introduce a large area of error. Due to the high sensitivity of the sensor, the EMI induced by the previously mentioned sources can potentially affect the turbulence data. The third source of error are the polyethylene seed particles present in the flow. When the sensing element is impacted by one of these particles, it can potentially cause an excitation which would be recorded as a random increase in pressure. The water tunnel itself also generated a relatively high background turbulence intensity. A previous study has shown that the average streamwise turbulence intensity value within the test section is ~3%, as measured using PIV [32]. This can destroy the eddies that are to be observed and, again, cause an increase in

flow disturbance that cannot be accounted for. The final source of error comes from the uncertainties found in the sensor itself. To obtain pressure data, the voltage values must be multiplied by a constant which is determined by the sensor's calibration curve. Therefore, converting from voltage to pressure induces a slight area of uncertainty which stems from the calibration curve.
Future work and means of mitigating these sources of error will be discussed in the following section.

8. CONCLUSION

The testing and verification of a state-of-the-art pressure sensor is paramount for both the manufacturer and consumer to be certain of its performance. The presented work increased understanding and provided insight into the abilities of the sensors developed by NanoSonic Inc., moving one step closer to a piezoresistive pressure sensor for underwater small scale pressure measurements. Throughout this paper the response of each sensor was investigated through multiple tests to highlight the ultrasensitive properties, and the following conclusions can be drawn:

- Each sensor displays good linearity with a high correlation coefficient
- Each sensor is capable of detecting small-scale pressure fluctuations of 0.04 inH_2O (~9.95 Pa)
- Testing in various environments highlight each sensor's ability to detect flow disturbances across the tested frequency range
- Testing in various environments exhibit the sensor's durability and ability to detect small-scale pressure fluctuations when in a semi-polluted environment

Present work has shown that the new pressure sensors are capable of detecting small-scale pressure measurements when in environments of minimal pressure differences. The static and dynamic calibration tests have shown that the sensor shows good linearity to match the overall detection range and that small-scale dynamic events can be observed and quantified. The stir and vortex shedding tests have shown the sensor response in the lower frequency regime, while the mid to high speaker test and turbulence decay test have demonstrated the sensors capability to perform in the upper frequency range up to 20kHz. The final, turbulence decay test, has provided valuable insight into the sensor's durability and also its ability to differentiate the small-scale pressure fluctuations when in a freestream and behind a turbulence generating grid.

Future research must be done to further validate the results of the turbulence decay test. The experiment can very easily be re-performed in a water tunnel with a lower background noise level and in a lab with less surrounding sources of EMI noise. In addition, the sensor should be mounted in an "L" shape, much like that of a Pitot tube, such that the sensing element is flush with the tip of the probe. This mounting configuration will create the least amount of flow disturbance around the sensing element allowing for more relevant data to be captured.

ACKNOWLEDGEMENTS

This material is based upon work in part supported by the U.S. Navy under contract N6833521C0262. We particularly acknowledge Dr. Derrick Custodio for his many insights and useful discussions of this work.

REFERENCES

[1] F. Xu et al., “Recent Developments for Flexible Pressure Sensors: A Review,” Micromachines, vol. 9, no. 11, p. 580, Nov. 2018, doi: 10.3390/mi9110580.

[2] Liwei Lin and Weijie Yun, "MEMS pressure sensors for aerospace applications," 1998 IEEE Aerospace Conference Proceedings (Cat. No.98TH8339), 1998, pp. 429-436 vol.1, doi: 10.1109/AERO.1998.686941.

[3] D. Tandeske, Pressure Sensors: Selection and Application. CRC Press, 1990, pp. v–13.

[4] Q. Meng, Y. Lu, J. Wang, D. Chen, and J. Chen, “A Piezoresistive Pressure Sensor with Optimized Positions and Thickness of Piezoresistors,” *Micromachines*, vol. 12, no. 9, p. 1095, Sep. 2021, doi: 10.3390/mi12091095.

[5] F. Ejeian *et al.*, “Design and applications of MEMS flow sensors: A review,” *Sensors and Actuators A: Physical*, vol. 295, pp. 483–502, Aug. 2019, doi: 10.1016/j.sna.2019.06.020.

[6] A. S. Morris and R. Langari, “Chapter 13 - Sensor technologies,” *ScienceDirect*, Jan. 01, 2021. https://www.sciencedirect.com/science/article/pii/B978012817141700013X

[7] Kumar, S.S., Pant, B.D. Design principles and considerations for the ‘ideal’ silicon piezoresistive pressure sensor: a focused review. Microsyst Technol 20, 1213–1247 (2014). https://doi.org/10.1007/s00542-014-2215-7

[8] W. Wang, X. He, X. Wang, M. Wang, and K. Xue, “A bioinspired structure modification of piezoelectric wind energy harvester based on the prototype of leaf veins,” *Sensors and Actuators A: Physical*, vol. 279, no. 0924-4247, pp. 467–473, Aug. 2018, doi: 10.1016/j.sna.2018.06.059.

[9] A. G. P. Kottapalli, M. Asadnia, J. M. Miao and M. S. Triantafyllou, "Harbor seal whisker inspired flow sensors to reduce vortex-induced vibrations," 2015 28th IEEE International Conference on Micro Electro Mechanical Systems (MEMS), 2015, pp. 889-892, doi: 10.1109/MEMSYS.2015.7051102.

[10] Bogue, R. (2013), "Recent developments in MEMS sensors: a review of applications, markets and technologies", Sensor Review, Vol. 33 No. 4, pp. 300-304. https://doi.org/10.1108/SR-05-2013-678

[11] J. O. Bird and P. J. Chivers, “49 - Measurement of fluid flow,” *ScienceDirect*, Jan. 01, 1993. https://www.sciencedirect.com/science/article/pii/B9780750616836500527

[12] C. B. Emmanuel and P. A. Mandics, *A Feasibility Study for the Remote Measurement of Underwater Currents Using Acoustic Doppler Techniques*. Environmental Research Laboratories, 1973. Accessed: Dec. 09, 2022. [Online].

[13] Z. Gong, C. Li, F. Jiang and J. Zheng, "AUV-Aided Localization of Underwater Acoustic Devices Based on Doppler Shift Measurements," in IEEE Transactions on Wireless Communications, vol. 19, no. 4, pp. 2226-2239, April 2020, doi: 10.1109/TWC.2019.2963296.

[14] C. Meurer, J. Francisco Fuentes-Pérez, N. Palomeras, M. Carreras and M. Kruusmaa, "Differential Pressure Sensor Speedometer for Autonomous Underwater Vehicle Velocity Estimation," in IEEE Journal of Oceanic Engineering, vol. 45, no. 3, pp. 946-978, July 2020, doi: 10.1109/JOE.2019.2907822.

[15] L. D. Chambers *et al.*, “A fish perspective: detecting flow features while moving using an artificial lateral line in steady and unsteady flow,” *Journal of The Royal Society Interface*, vol. 11, no. 99, p. 20140467, Oct. 2014, doi: 10.1098/rsif.2014.0467.

[16] J. H. Kepper, B. C. Claus and J. C. Kinsey, "A Navigation Solution Using a MEMS IMU, Model-Based Dead-Reckoning, and One-Way-Travel-Time Acoustic Range Measurements for Autonomous Underwater Vehicles," in IEEE Journal of Oceanic Engineering, vol. 44, no. 3, pp. 664-682, July 2019, doi: 10.1109/JOE.2018.2832878.

[17] Y. Bi, X. Xu, S. Chua, E. Chow, and X. Wang, “Underwater Turbulence Detection Using Gated Wavefront Sensing Technique,” *Sensors*, vol. 18, no. 3, p. 798, Mar. 2018, doi: 10.3390/s18030798.

[18] MS54XX miniature SMD pressure sensor - AMSYS gmbh & co.. KG, https://www.amsys-sensor.com/downloads/data/MS54XX-AMSYS-datasheet.pdf (accessed May 8, 2023).

[19] Kottapalli, Ajay Giri Prakash & Asadnia, Mohsen & Miao, Jianmin & Tan, C.W. & Barbastathis, G. & Triantafyllou, Michael. (2012). Polymer MEMS pressure sensor arrays for fish-like underwater sensing applications. Micro & Nano Letters, IET. 7. 1189-1192. 10.1049/mnl.2012.0604.

[20] A. P. De Clerck, “Modeling the Thermal Performance of an Intelligent MEMS Pressure Sensor with Self-Calibration Capabilities,” *vtechworks.lib.vt.edu*, Oct. 23, 2020. https://vtechworks.lib.vt.edu/handle/10919/100688 (accessed Dec. 09, 2022).

[21] D. Duraibabu et al., “An Optical Fibre Depth (Pressure) Sensor for Remote Operated Vehicles in

Underwater Applications," Sensors, vol. 17, no. 2, p. 406, Feb. 2017, doi: 10.3390/s17020406.

[22] Cattaneo L. Fancies and Fallacies of Spatial Sampling With Transcranial Magnetic Stimulation (TMS). Front Psychol. 2018 Jul 5;9:1171. doi: 10.3389/fpsyg.2018.01171. PMID: 30026721; PMCID: PMC6042252.

[23] "H2a-XLR Hydrophone User's Guide." Accessed: Dec. 09, 2022. [Online]. Available: https://www.aquarianaudio.com/AqAudDocs/H2a_XLR_manual.pdf

[24] "Lubell LL916 Underwater Speaker or Underwater Loudspeaker," *www.lubell.com*. https://www.lubell.com/LL916.html (accessed Dec. 09, 2022).

[25] M. Laroussi, M. Djebbi, and M. Moussa, "Triggering vortex shedding for flow past circular cylinder by acting on initial conditions: A numerical study," *Computers & Fluids*, vol. 101, pp. 194–207, Sep. 2014, doi: 10.1016/j.compfluid.2014.05.034.

[26] R. L. Panton, *Incompressible flow*. Hoboken, Nj Wiley, 2013.

[27] C. S. Greco, G. Paolillo, T. Astarita, and G. Cardone, "The von Kármán street behind a circular cylinder: flow control through synthetic jet placed at the rear stagnation point," Journal of Fluid Mechanics, vol. 901, p. A39, 2020.

[28] R. D. Gabbai and H. Benaroya, "An overview of modeling and experiments of vortex-induced vibration of circular cylinders," *Journal of Sound and Vibration*, vol. 282, no. 3–5, pp. 575–616, Apr. 2005, doi: 10.1016/j.jsv.2004.04.017.

[29] P. E. Roach, "The generation of nearly isotropic turbulence by means of grids," *International Journal of Heat and Fluid Flow*, vol. 8, no. 2, pp. 82–92, Jun. 1987, doi: 10.1016/0142-727x(87)90001-4.

[30] H. Yao, L. Cao, D. Wu, Y. Gao, S. Qin, and F. Yu, "PIV Study on Grid-Generated Turbulence in a Free Surface Flow," Water, vol. 13, no. 7, p. 909, Mar. 2021, doi: 10.3390/w13070909.

[31] T. Kurian1 and J. H. M. Fransson, "IOPscience," Fluid Dynamics Research, https://iopscience.iop.org/article/10.1088/0169-5983/41/2/021403/meta (accessed May 8, 2023).

[32] A. Borgoltz, M. Szoke, W. George, and T. Meyers, "Experiment 4 - Particle Shadow Velocimetry," *www.dept.aoe.vt.edu*, Sep. 14, 2021. http://www.dept.aoe.vt.edu/~aborgolt/aoe3054/manual/expt4/index.html

[33] M. H. Same, G. Gandubert, G. Gleeton, P. Ivanov, and R. Landry, "Simplified Welch Algorithm for Spectrum Monitoring," Applied Sciences, vol. 11, no. 1, p. 86, Dec. 2020, doi: 10.3390/app11010086.

[34] N. D. Merchant, T. R. Barton, P. M. Thompson, E. Pirotta, D. T. Dakin, and J. Dorocicz, "Spectral probability density as a tool for ambient noise analysis," *The Journal of the Acoustical Society of America*, vol. 133, no. 4, pp. EL262–EL267, Apr. 2013, doi: 10.1121/1.4794934.

APPENDIX A: DYNAMIC EVENTS OBSERVATIONS

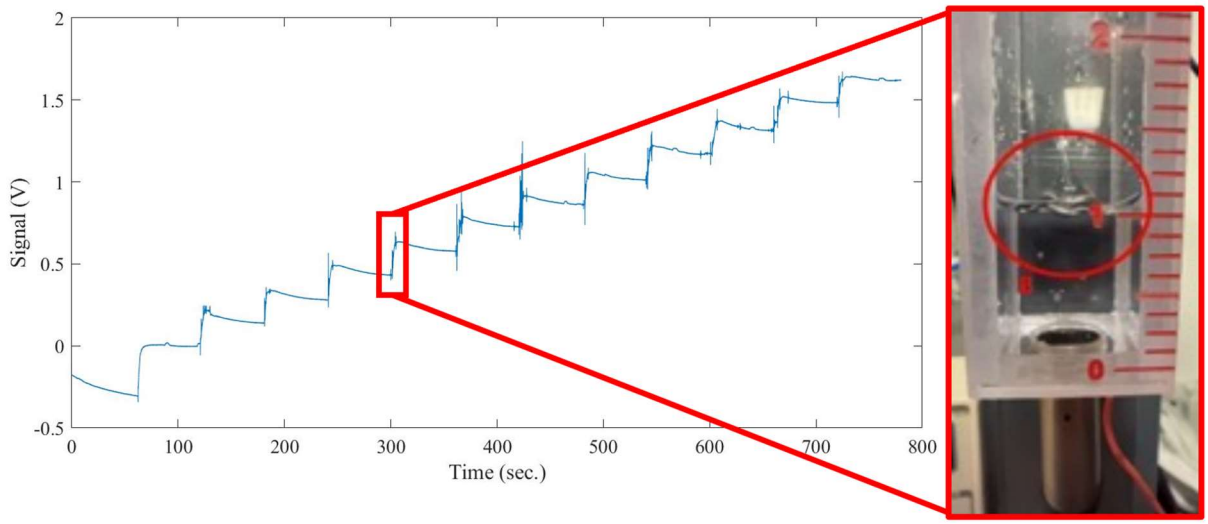

Figure 23: Time history data characterizing the performance of sensor 5 during dynamic calibration and a view of the surface fluctuations caused by a falling water droplet

During the sensor calibration process, a preliminary test was performed to exhibit the excitation of the sensor in response to a minimal pressure change. No quantitative results were computed. Data was recorded as the water height was increased from 0" to 6" in 0.5" increments when water was falling from a height of 9.75" in order to observe water surface fluctuations. The water was dispensed into the column using a pipette.

As the water was deposited into the column, it created small-scale disturbances on the surface, minimally changing the overall applied pressure to the sensor. The figure above demonstrates the time domain sensor response and clarifies the behavior of the water when dropped from a height of 9.75".

The red circle contained within Figure 23 also depicts a small volume of water being forced upwards when the surface was subjected to fluctuations, which can be used to characterize the slight decrease in voltage output from the sensor. The sensor displayed an excitation of about 0.2V lasting for the time period of surface fluctuations (about 200ms). The minimal pressure differences generated by water surface fluctuations were detected by the sensor, hence further displaying its ultrasensitive properties.

APPENDIX B: POWER SPECTRUM

The energy/power spectrum is a useful tool to describe how the energy in a signal is distributed with frequency. Consider a fluctuating signal, $x(t)$. In the frequency domain, the one-dimensional energy spectrum can be drawn using Equation 4:

$$E(f) = \lim_{T \to \infty} \frac{|X_T(f)|^2}{T} \tag{4}$$

Where $X_T(f)$ is the Fourier transform of T seconds of $x(t)$. In engineering applications, the most common method of estimating the energy spectrum is the segment averaging approach, also known as Welch's method. This method divides (or segments) the signal into blocks in time, that can overlap as much as 50% [33]. At each block, a Fourier transform is computed, and the magnitude is squared (also known as a periodogram), from which averaging the results obtain the final power spectrum estimate.

APPENDIX C: POWER SPECTRUM COMPARISON

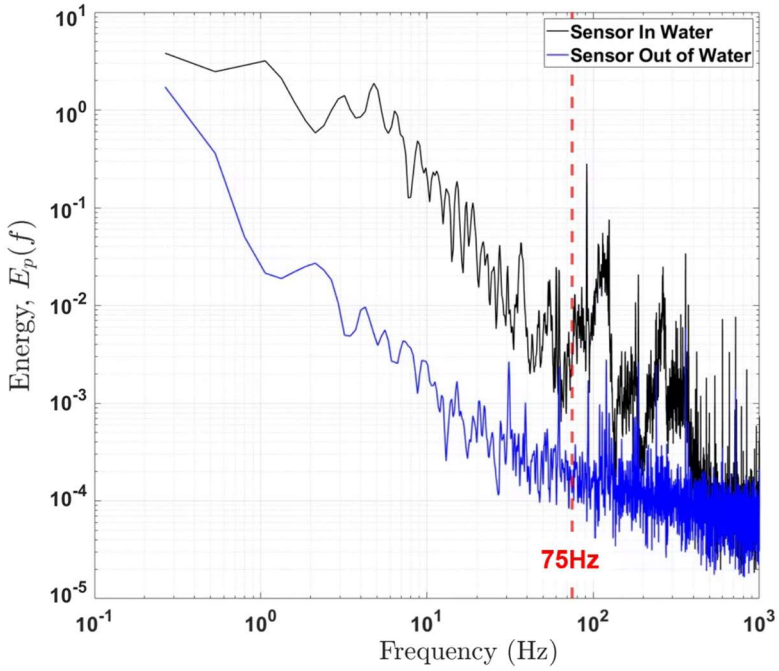

Figure 24: The power spectrum drawn when the water tunnel pump was turned on and when the sensor was both out the water (blue) and 5" downstream of the grid (black)

As mentioned, the power spectrum was calculated using MATLAB's built-in "pwelch" function, with 8 segments and 50% overlap. To establish an appropriate sampling rate, measurements were taken with the water tunnel pump in operation and the sensor positioned outside of the water, and the resulting power spectrum was compared to that taken at a location 5 inches downstream of the turbulence generating grid, as illustrated in Figure 24. As shown, the power spectrum obtained with the sensor outside of the water (blue) revealed substantial peaks, including irregular and prominent ones beyond the 75Hz threshold, which were replicated in the power spectrum derived from measurements taken with the sensor immersed in water (black). Hence, the Nyquist frequency was determined as 75Hz, and a sampling rate of 150Hz was deemed acceptable.

APPENDIX D: RESAMPLING STUDY

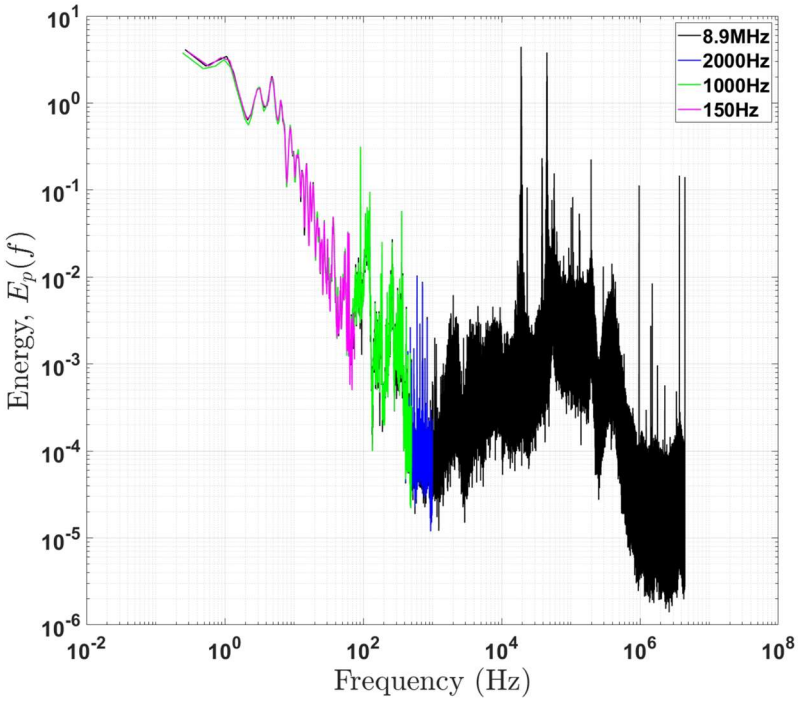

Figure 25: The calculated power spectrum 5" downstream of the turbulence generating grid at different sampling rates

Determining a proper sampling rate is a critical step to ensure the obtained results are as accurate as possible. Multiple sources in literature use the turbulence energy spectrum, or the power spectrum of the fluctuating velocity signal, as a means to get this. This approach was followed using the obtained pressure data, and the power spectrum was calculated using the pressure data obtained 5 inches downstream of the grid which can be seen in Figure 25. Many jagged and abrupt peaks can be seen throughout the entire frequency range, which are indicative of noise in the measurements. But, as the sampling rate decreases, so does the span of the spectrum. Therefore, an appropriate sampling rate can be chosen such that many of the peaks can be eliminated. At ~1kHz lies a "noise floor", denoting that any higher frequencies contain noise that is introduced by the sensitivity of the sensor [34]. When the data is resampled to 150Hz, the data contained within the large peaks are eliminated, as well as data which lies past the noise floor (~1kHz).

To summarize, down sampling the data to 150Hz causes the span of the spectrum to decrease such that the jagged and abrupt peaks present at ~100Hz are eliminated following the previously mentioned reasoning. Therefore, a 150Hz sampling rate was seen as sufficient, and was applied to all data sets obtained through the experiment.